Noninvasive imaging of tumor progression, metastasis, and fibrosis using a nanobody targeting the extracellular matrix

Noor Jailkhani[a], Jessica R. Ingram[b,1], Mohammad Rashidian[c], Steffen Rickelt[a], Chenxi Tian[a], Howard Mak[a], Zhigang Jiang[a], Hidde L. Ploegh[c], and Richard O. Hynes[a,d,2]

[a]Koch Institute for Integrative Cancer Research, Massachusetts Institute of Technology, Cambridge, MA 02139; [b]Department of Cancer Immunology and Virology, Dana Farber Cancer Institute, Boston, MA 02115; [c]Program in Molecular and Cellular Medicine, Boston Children's Hospital, Boston, MA 02115; and [d]Howard Hughes Medical Institute, Massachusetts Institute of Technology, Cambridge, MA 02139

Contributed by Richard O. Hynes, March 24, 2019 (sent for review October 10, 2018; reviewed by Peter Caravan and Yibin Kang)

Extracellular matrix (ECM) deposition is a hallmark of many diseases, including cancer and fibroses. To exploit the ECM as an imaging and therapeutic target, we developed alpaca-derived libraries of "nanobodies" against disease-associated ECM proteins. We describe here one such nanobody, NJB2, specific for an alternatively spliced domain of fibronectin expressed in disease ECM and neovasculature. We showed by noninvasive in vivo immuno-PET/CT imaging that NJB2 detects primary tumors and metastatic sites with excellent specificity in multiple models of breast cancer, including human and mouse triple-negative breast cancer, and in melanoma. We also imaged mice with pancreatic ductal adenocarcinoma (PDAC) in which NJB2 was able to detect not only PDAC tumors but also early pancreatic lesions called pancreatic intraepithelial neoplasias, which are challenging to detect by any current imaging modalities, with excellent clarity and signal-to-noise ratios that outperformed conventional 2-fluorodeoxyglucose PET/CT imaging. NJB2 also detected pulmonary fibrosis in a bleomycin-induced fibrosis model. We propose NJB2 and similar anti-ECM nanobodies as powerful tools for noninvasive detection of tumors, metastatic lesions, and fibroses. Furthermore, the selective recognition of disease tissues makes NJB2 a promising candidate for nanobody-based therapeutic applications.

cancer | ECM | nanobodies | PET imaging | fibrosis

Metastasis is the major cause of mortality from cancer, and patients often present with advanced-stage disease. Although early detection of tumors and metastatic lesions can significantly improve survival and reduce cancer burden, it remains a major clinical challenge (1). Metastatic potential of tumors is hard to predict, and there are currently no therapeutic strategies specifically targeting obvious or occult metastases (2). There is clearly an unmet need to develop novel diagnostic, imaging, and therapeutic strategies to detect and target tumors, especially early-stage lesions and metastases.

The extracellular matrix (ECM) forms a major component of the tumor microenvironment, providing biochemical and biomechanical support (3). Cell–ECM interactions play major roles in invasion, cell survival, enhanced angiogenesis, and resistance to chemo- and radiotherapies (4–6). ECM is remodeled in development and in many diseases, including cancer, and often contains proteins and/or domains of ECM proteins that are selectively and/or abundantly present at disease sites (7–10). This selective abundance makes ECM proteins promising candidates for the development of diagnostic and therapeutic approaches in cancer and other disorders characterized by ECM remodeling and deposition.

Imaging and targeting of ECM proteins in cancer offer several advantages over existing methods. Therapies that target tumor cells can have limited efficacy as a result of tumor cell heterogeneity and genomic instability of tumor cells. In addition, resistance can also arise as a result of other mechanisms, such as alteration in target expression and drug efflux (11). In cancer, ECM proteins rarely have mutations, and ECM-targeted approaches will not be challenged by immune evasion mediated by immune editing. The readily accessible extracellular position, abundance, stability, and characteristic patterns of distribution of ECM proteins make them particularly attractive targets. Monoclonal antibodies and recombinant single-chain variable fragment (scFv) antibodies against ECM proteins have been used to target tumor vasculature with some success (12, 13).

In addition to cancer, ECM remodeling and deposition are also characteristic of a number of other diseases, and at least some of the ECM biomarkers are shared among these diseases (7). These include (but are not limited to) cardiovascular disorders (such as atheroma, aneurysms, and myocardial infarction), as well as fibrotic and inflammatory disorders (7, 14, 15). Therapies and detection tools developed against such ECM-specific targets will have potential for use as broad-acting targeting agents, as target-antigen expression will not be restricted to a single cancer or disease type.

We and others have developed proteomic methods for defining in detail the ECM composition of multiple cancer types, their metastases, and other diseased tissues (7–10, 16). These datasets provide a rich resource of potential ECM targets. There are hundreds of ECM and ECM-associated proteins encoded in mammalian

Significance

Cancers, fibroses, and inflammatory disorders are characterized by increased deposition of the extracellular matrix (ECM). ECM biomarkers that are selectively expressed at these disease sites are attractive targets for imaging and therapeutic approaches. Nanobodies against these biomarkers would be pertinent vehicles for the accumulation of imaging and therapeutic cargo at disease sites, potentially increasing specificity and reducing background. We demonstrate the specificity of one such anti-ECM nanobody by using immuno-PET/CT and show that it detects multiple models of cancer, including early lesions and metastases, and also fibroses, with excellent specificity and clarity. Thus, novel strategies for delivering imaging and therapeutic probes specifically to the ECM in disease sites may prove particularly valuable for detection and treatment of cancer in patients.

Author contributions: N.J., J.R.I., and R.O.H. designed research; N.J., M.R., S.R., C.T., H.M., and Z.J. performed research; J.R.I., M.R., C.T., and H.L.P. contributed new reagents/analytic tools; N.J. and R.O.H. analyzed data; and N.J. and R.O.H. wrote the paper.

Reviewers: P.C., Massachusetts General Hospital, Harvard Medical School; and Y.K., Princeton University.

The authors declare no conflict of interest.

[1]Deceased April 18, 2018.

[2]To whom correspondence should be addressed. Email: rohynes@mit.edu.

This article contains supporting information online at www.pnas.org/lookup/suppl/doi:10.1073/pnas.1817442116/-/DCSupplemental.

Published online May 8, 2019.

genomes, and any given tissue expresses at least 150–200 of them, many of which change during cancer progression and in other disease states. Furthermore, a good number of those are overexpressed in multiple cancers and in other disease states (6, 16). To develop libraries of immune reagents against these diverse ECM targets, we have used nanobody methods. Nanobodies are single-domain variable regions (VHHs) derived from camelid heavy-chain–only antibodies (17) and have significant advantages over other antibody formats for in vivo diagnostic imaging and targeted delivery. Their small size (~15 kDa) allows deeper tissue penetration and faster renal clearance than larger antibody reagents. Nanobodies are reported to be poorly immunogenic and highly stable (17, 18). We hypothesized that imaging probes and therapeutic cargo tagged to nanobodies specific for disease-associated ECM proteins would selectively accumulate in tumors and metastatic sites, resulting in increased specificity and sensitivity of detection and treatment, while reducing background and off-target systemic toxicity.

Here we describe the development of diverse nanobody libraries against ECM proteins associated with cancer and other diseases. We illustrate the broad utility of such reagents by using an ECM-specific nanobody, NJB2, recognizing the alternatively spliced EIIIB (EDB) domain of fibronectin (FN) (19), a glycoprotein that forms a major constituent of tumor ECM and neovasculature (20, 21). Although the physiological roles of EIIIB remain unclear; it is widely expressed in cancers, fibroses, atheromas, aneurysms, and other diseases characterized by ECM deposition and is nearly absent from most normal adult human tissues (22–24). What makes EIIIB particularly useful in the context of our work is the fact that its sequence is identical in mice and humans. By using two-photon immunofluorescence and noninvasive immuno-PET/CT imaging, we demonstrate the application of NJB2 to detect and image tumors, metastases, and fibroses with good specificity and sensitivity and, in the case of cancer, with higher signal-to-noise ratios than conventional ^{18}F-2-fluorodeoxyglucose (FDG) PET/CT imaging.

Results

Generation of ECM-Targeted Nanobody Libraries. To develop nanobodies against diverse ECM-associated proteins of interest, we generated four different nanobody libraries. Library A was made from an alpaca immunized with a mixture of ECM proteins including full-length ECM proteins, domains of ECM proteins, and peptides derived from ECM proteins (Fig. 1*A*). The other three libraries (B, C, D) were derived from alpacas immunized with ECM-enriched preparations from patient samples of colorectal cancer metastases to the liver and triple-negative breast cancer (TNBC) metastases to the liver or lung. Following immunization of alpacas, lymphocytes were purified from their peripheral blood. RNA was extracted and reverse-transcribed to cDNA, and VHH regions were amplified by PCR and cloned into phagemid vectors to generate phage-display libraries (Fig. 1*A*). The composition, diversity, and use of libraries B, C, and D will be described in greater detail elsewhere.

Generation and in Vitro Validation of NJB2, a High-Affinity FN-EIIIB–Specific Nanobody. In tumor stroma and neovasculature, FN undergoes alternative splicing. The inclusion of alternatively spliced exons results in FN that contains the EIIIA and EIIIB domains (20, 21, 23, 25, 26). Relatively selective expression of EIIIA and EIIIB in the ECM of tumors and metastases and the abundance of FN in disease stroma make EIIIB a promising candidate for the development of selective nanobody-based imaging and targeting strategies. Library A was used to isolate nanobodies against the EIIIB domain of FN. After two rounds of panning, we selected ELISA-positive clones that bound EIIIB. Nanobodies were sequenced and subcloned and proteins were produced. To validate their specificity, we installed biotin at the C termini of the nanobodies

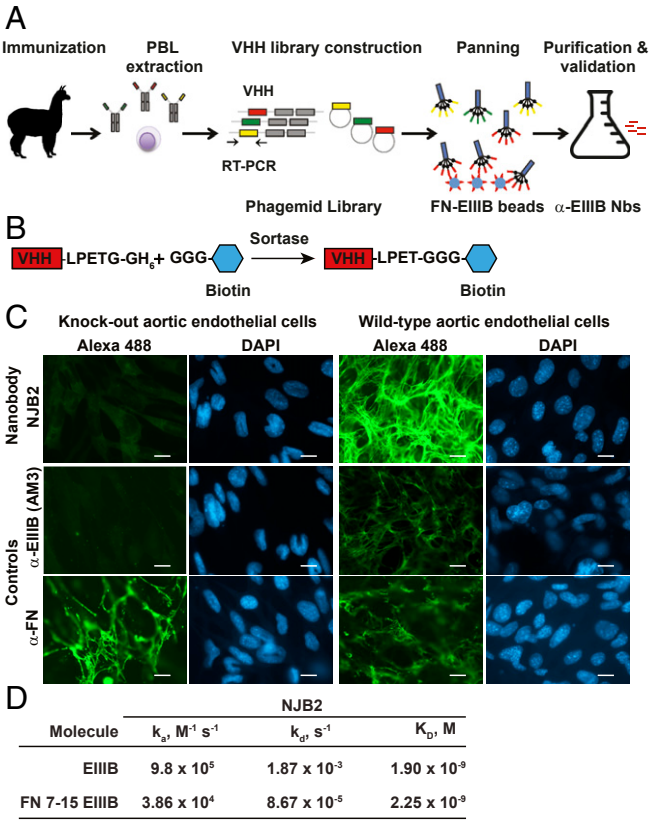

Molecule	k_a, M^{-1} s^{-1}	k_d, s^{-1}	K_D, M
EIIIB	9.8×10^{5}	1.87×10^{-3}	1.90×10^{-9}
FN 7-15 EIIIB	3.86×10^{4}	8.67×10^{-5}	2.25×10^{-9}

Fig. 1. Generation and in vitro characterization of FN-EIIIB–specific nanobody NJB2. (*A*) Four different alpacas were immunized with a mixture of ECM proteins or with ECM-enriched preparations from patient metastasis samples (*SI Appendix, Materials and Methods*). Following immunization, peripheral blood lymphocytes (PBLs) were purified and used to generate VHH phage-display libraries. EIIIB-specific nanobodies (Nbs) were selected from the library generated with a mix of ECM proteins and peptides (library A) after two rounds of phage panning. (*B*) Nanobodies are expressed with a C-terminal sortase-recognition motif (LPETG), followed by a 6xHis tag to facilitate purification. The sortase motif allows sortase-mediated, site-specific addition of probes with an N-terminal poly-glycine by transpeptidation at the threonine–glycine bond. (*C*) NJB2 was site-specifically labeled with biotin via sortagging (*B*) and detected with Streptavidin-Alexa 488. (*C*, *Right*) NJB2 specifically recognizes the EIIIB domain of FN in the ECM of WT aortic endothelial cells. (*C*, *Left*) However, it did not recognize FN in the ECM of endothelial cells genetically lacking the EIIIA and EIIIB domains of FN. Controls are cells stained with AM3 anti-EIIIB monoclonal antibody or α-FN polyclonal antibody. (Scale bars, 100 μm.) (*D*) Binding of NJB2 to immobilized EIIIB-domain–containing fragments measured by using biolayer interferometry. K_D, k_a, and k_d values.

by sortase-mediated transacylation (i.e., "sortagging"; Fig. 1*B*). We tested binding of the VHHs to different FN fragments (with and without EIIIB domain) to validate specificity for FN containing EIIIB by immunoblot. The best of these nanobodies, NJB2, recognized all fragments that contained EIIIB but not human plasma FN (*SI Appendix*, Fig. S1*A*). NJB2 also recognized EIIIB by ELISA and in immunohistochemistry (IHC; *SI Appendix*, Fig. S1 *B* and *C*).

We further demonstrated that NJB2 recognized full-length FN containing EIIIB in ECM produced by murine aortic endothelial cells WT for FN-EIIIA and EIIIB domains but not in the ECM of cells that were KOs for these domains (Fig. 1*C*). These results were similar to staining observed with the antibody AM3, a mouse monoclonal IgG against EIIIB (27).

The binding affinity of NJB2 for EIIIB was measured by biolayer interferometry. We tested two different fragments containing EIIIB (28, 29) and observed that NJB2 bound immobilized

single EIIIB domain (EIIIB) and a large recombinant rat FN fragment comprising FNIII7–15, including EIIIB (FN 7–15 EIIIB), with K_D values of 1.9×10^{-9} M and 2.25×10^{-9} M, respectively (Fig. 1*D*).

NJB2 Nanobody Selectively Binds Tumor ECM in Vivo in Primary Tumors and Lung Metastases in a TNBC Model. To test whether NJB2 binds to FN-EIIIB in the ECM of tumors and metastases in vivo, we tagged the nanobody with Texas Red using sortagging (30). LM2-TGL-ZsGreen cells (1×10^6) were injected in the fourth mammary fat pad or via tail vein in NOD/SCID/gamma (NSG) mice. At 2.5 wk, control mice (no tumor) and mice with tumors and metastases were injected i.v. with NJB2-Texas Red and euthanized 2 h postinjection, and organs were resected and imaged by two-photon microscopy. In the primary tumors and lung metastases, NJB2 localized specifically to ECM fibrils surrounding the ZsGreen-expressing tumor cells, but not to the ECM in normal lung parenchyma (Fig. 2*A*, "N"). *Z*-stacks were acquired to different depths (up to ~150 μm) into the tissues, and clear signals from the tumor and metastatic ECM were visible even at depths of 150 μm, indicating excellent tissue penetration of NJB2. No binding was seen in the livers from any mice or in the lungs of control mice or mice with primary tumors (Fig. 2*A*). These results confirmed that, at 2 h postinjection, NJB2 binds specifically to the ECM of tumors and metastases in vivo.

^{64}Cu–Labeled NJB2 Detects Tumors and Metastases in Vivo by Immuno-PET/CT in a TNBC Model. To test whether direct molecular imaging of FN-EIIIB with NJB2 can be used for noninvasive detection and targeting of tumors and metastases, we used immuno-PET/CT with ^{64}Cu-labeled NJB2. We followed a previously described antibody-labeling strategy (31). Briefly, by using sortase-mediated transpeptidation, a NOTA-$(Gly)_3$ nucleophile was conjugated to the C terminus of the LPXTG-modified nanobody and mixed with a solution of $^{64}Cu^{2+}$ to yield ^{64}Cu-NJB2. ^{64}Cu has a $t_{1/2}$ of ~12.7 h, which allows extended in vivo imaging and monitoring of nanobody binding.

Control NSG mice (no tumors) and mice bearing primary tumors or pulmonary metastases derived from LM2-TGL-ZsGreen cells were injected with ^{64}Cu-NJB2 and imaged 2 h later using PET followed by CT for anatomical reference. Control mice showed signal in some organs of elimination (kidney, bladder) and signal at lower levels in intestine and liver (Fig. 2 *B* and *D*); ^{64}Cu is known to undergo hepatobiliary clearance, and liver signals have been previously reported for ^{64}Cu-labeled antibodies (32). However, ^{64}Cu-NJB2 detected tumors or metastases with clarity and high signal-to-noise ratio, indicating specificity and homing to the EIIIB target (Fig. 2*B*). The in vivo PET signals at 2 h post injection were quantified as PET standardized uptake value (SUV), and tissue-to-muscle ratios (TMRs) were calculated (Fig. 2*C* and *SI Appendix*, Fig. S2). The uptake in tumors and lung metastases was significantly higher than in mammary fat pads and lungs of control mice as observed from TMR (Fig. 2*C*). All other organs including liver showed no significant differences. To examine persistence at the target site, mice bearing primary tumors were also imaged 24 h after NJB2 injection. The TMR of the primary tumors was lower at 24 h than at 2 h after nanobody injection, but it remained significantly higher than in controls, indicating that the nanobody remained bound to the tumor ECM even 24 h after administration. This decrease in primary tumor signal over 24 h may be a result of biological turnover of the ECM or hydrolysis of the nanobody–NOTA–^{64}Cu conjugate.

Mice were euthanized after imaging, and organs were resected for biodistribution analysis. The ex vivo biodistribution, calculated as percentage of injected dose per gram (%ID/g), was similar in most organs except for primary tumors and lungs with metastases, which had significantly higher uptake of NJB2 than the fat pads and lungs of control mice (Fig. 2*D*). The significantly higher tissue-to-blood ratios of 16.9 for primary tumors and 5.9 for lung metastases further establish the NJB2 nanobody as a promising tool for in vivo applications (Fig. 2*D*, *Inset*). The specificity of ^{64}Cu-NJB2 was further demonstrated when tumor-bearing

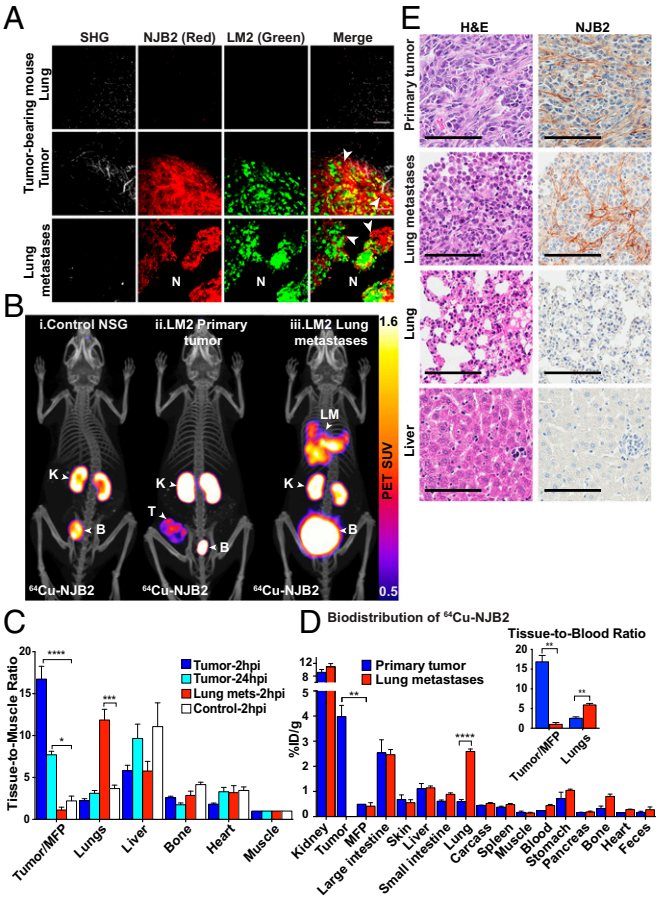

Fig. 2. NJB2 nanobody detects ECM in primary tumors and lung metastases in a breast cancer model. (*A*) Control mice (no tumor) and mice with primary tumors and lung metastases derived from LM2-TGL-ZsGreen cells were injected with NJB2-Texas Red. Organs were resected 2 h after nanobody injection and imaged by using two-photon microscopy. Representative images are shown as an overlay of different channels. The nanobody bound ECM of primary tumors and lung metastases (arrowheads) but not normal tissue ECM (marked as "N"). SHG, second harmonic generation. (Scale bars, 100 μm.) (*B*) NSG mice were injected with 1×10^6 LM2 cells in the mammary fat pad (MFP) or via the tail vein to induce primary tumors or pulmonary metastases. Four weeks later, mice were injected with ^{64}Cu-NJB2 and imaged 2 h postinjection (hpi) with PET/CT. Mice with primary tumors were also imaged 24 h postinjection. Representative PET/CT images of (*i*) NSG control mice; signals detected in kidney ("K") and bladder ("B") and also in intestine and liver (Fig. 2*D*). (*ii*) Mouse bearing primary tumor; strong signals also detected in primary tumor ("T"). (*iii*) Mouse bearing pulmonary metastases; strong signals also detected in lung metastases ("LM"). Movies S1–S3 show 3D rendering. (*C*) Quantification of radioactivity in vivo (decay-corrected) at 2 and 24 h postinjection of ^{64}Cu-NJB2 calculated as TMRs of PET SUV for the indicated organs (blue bars, mice bearing primary tumors; red bars, mice with lung metastases; white bars, controls). Data were analyzed by using one-way ANOVA, followed by post hoc Tukey's multiple comparison tests ($n = 3$ mice with primary tumors; $n = 4$ mice with lung metastases; $n = 2$ controls). (*D*) Ex vivo biodistribution of ^{64}Cu-NJB2 in organs of mice with primary tumors (blue bars) and mice with lung metastases (red bars), expressed as %ID/g (mean ± SE) in various organs 150 min after injection. (*Inset*) Same data as in *D* expressed as a ratio of tissue to blood. Data were analyzed by two-tailed unpaired *t* test ($n = 3$ for both groups). (*E*) Expression of EIIIB at the tumors and metastatic sites was confirmed by H&E staining and IHC using NJB2-biotin. (Scale bars, 100 μm.)

mice injected with the irrelevant nontargeting control nanobody 96G3M (33) did not show any uptake at the tumor site (*SI Appendix*, Fig. S3). Administration of 100-fold excess of unlabeled NJB2 before imaging with ^{64}Cu-NJB2 resulted in a significant decrease in PET signal from the tumor (*SI Appendix*, Fig. S3).

The excised tissues were processed for H&E staining and IHC with NJB2-biotin (Fig. 2*E*). NJB2 bound to ECM fibers in the stroma of tumors and lung metastases, but no staining was observed in the ECM of normal lungs and liver.

^{64}Cu–NJB2 Detects Discrete Metastases to Liver and Lymph Nodes, with Superior Signal-To-Noise Ratio than ^{18}F-FDG PET/CT in a Mouse Model of Spontaneous Metastasis. Compared with the pulmonary metastasis model, in which cells are directly injected into the tail vein, the spontaneous metastasis model is more similar to metastases observed in patients. We used ^{64}Cu-NJB2 PET/CT to image control mice and mice with LM2-TGL-ZsGreen–derived orthotopic tumors allowed to grow and metastasize for 6 wk to form discrete metastases in multiple organs (Fig. 3*A*, *Top*). For comparison, mice were also imaged with ^{18}F-FDG, the principal imaging agent used clinically for noninvasive diagnosis and staging of tumor progression and metastasis (Fig. 3*A*, *Lower*). PET/CT with ^{18}F-FDG is based on the increased uptake of ^{18}F-FDG by metabolically active cells, and, although widely used, has several limitations (34). ^{64}Cu–NJB2 detected the orthotopic tumor and the discrete liver and lymph node (LN) metastases (LN Met) with clarity and specificity. The ^{18}F-FDG detected the primary tumors and liver metastases, albeit with less specificity than did ^{64}Cu-NJB2, but ^{18}F-FDG PET/CT failed to clearly visualize LN Met (Fig. 3*A*).

The in vivo PET signals were quantified (Fig. 3*B* and *SI Appendix*, Fig. S4). The TMR with ^{64}Cu-NJB2 was consistently and significantly higher for tumors and metastatic sites, indicating increased uptake compared with other organs (Fig. 3*B*). Compared with ^{18}F-FDG, the TMR with ^{64}Cu-NJB2 was 6.5-fold higher for LN Met, approximately fourfold higher for liver metastases, and threefold higher for the primary tumor. We saw no significant differences in lungs or bone.

Following PET/CT imaging, mice were euthanized and their organs resected for fluorescence imaging and histopathological analysis. To assess the size of the smallest metastatic lesion detected by ^{64}Cu-NJB2, fluorescence image analysis of the metastatic organs (lung, liver, LNs) showed that the ^{64}Cu-NJB2 clearly detected metastases larger than ∼2.5 mm (Fig. 3*C* and *SI Appendix*, Fig. S5). In these experiments, neither ^{64}Cu-NJB2 nor ^{18}F-FDG detected metastatic lesions smaller than ∼2.5 mm in diameter (*SI Appendix*, Fig. S5). H&E staining of the orthotopic tumors showed necrotic regions in the core of the tumor surrounded by live tumor cells (Fig. 3*D*, *Left*). IHC with NJB2 showed the presence of ECM fibrils in the stroma in the live regions of the tumor, with few to no fibrils in the necrotic regions. The IHC conforms with the in vivo ^{64}Cu-NJB2 PET/CT signal, which is stronger in the tumor periphery than in the tumor core (Fig. 3*A*). H&E staining of the liver metastases marked as "LM2" in Fig. 3 showed that the ECM distribution in metastases was evidently different from the ECM of the adjacent normal liver (Fig. 3*D*, *Center*). IHC with NJB2 showed that ECM containing EIIIB was present throughout the stroma of the liver metastases (including the center) and showed a clear demarcation between the normal and diseased stroma at the edge of the metastatic nodule. Strong ECM staining was also observed in the ECM of LN Met (Fig. 3*D*, *Right*). These results further validate that NJB2 binds specifically to FN containing EIIIB in the ECM of tumors and metastatic sites but not to FN in normal liver parenchyma.

^{64}Cu–NJB2 Nanobody in Early Detection of Pancreatic Ductal Adenocarcinoma. Pancreatic ductal adenocarcinoma (PDAC) develops through well-defined neoplastic stages and is characterized by increasing desmoplasia and prominent ECM deposition

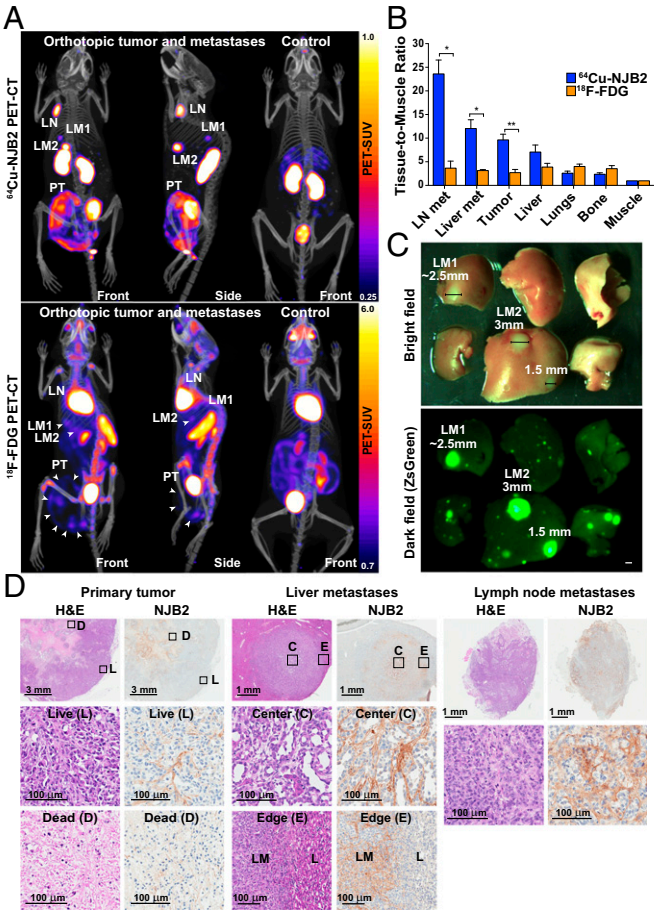

Fig. 3. NJB2 nanobody detects discrete metastases to liver and LNs with a higher signal-to-noise ratio compared with ^{18}F-FDG PET/CT imaging. (*A*) NSG mice were injected in the mammary fat pad with 0.25×10^6 LM2 cells. The tumors were allowed to grow and metastasize for 6 wk. Mice were imaged with ^{18}F-FDG or ^{64}Cu-NJB2. The ^{64}Cu-NJB2 PET/CT images were compared with ^{18}F-FDG images of the same mouse. Representative PET/CT images (front and side views) imaged with ^{64}Cu-NJB2 reveal primary tumor (PT), discrete LN, and liver metastases (LM1, LM2). In ^{18}F-FDG PET/CT, signals were observed in the primary tumor (PT), heart, kidney, spleen, bladder, and Harderian glands. Movies S4–S7 show 3D visualization. (*B*) In vivo PET signals were quantified 2 h after injection of ^{64}Cu-NJB2 and 90 min after injection of ^{18}F-FDG. ^{64}Cu–NJB2 was able to detect primary tumors and metastases with a significantly higher TMR compared with ^{18}F-FDG PET/CT. Data were analyzed by two-tailed unpaired *t* test. ($n = 3$ for mice with orthotopic tumors; *SI Appendix*, Fig. S4). (*C*) Bright-field and fluorescence microscopy of resected liver lobes with metastases (*SI Appendix*, Fig. S5). (Scale bar, 1 mm.) (*D*) H&E staining and IHC with NJB2 of resected organs of mice imaged in *A*. EIIIB was observed in the ECM surrounding live tumor cells (marked as "L") but not in the dead/necrotic regions ("D"). Strong EIIIB staining was observed in the ECM of liver metastases (LM) and LN Met but not in the ECM of normal liver ("L").

(35). PDAC progression from initiation to metastatic disease can take nearly two decades, suggesting a wide window of opportunity for early detection (36). We were interested in testing whether NJB2 can be used for early detection and tracking of PDAC progression. We used the KPC mouse models of PDAC (37, 38), which recapitulate different stages of PDAC progression including pancreatic intraepithelial neoplasias (PanINs), which are precursor lesions that progress to PDAC. To test the expression of EIIIB during PDAC progression, we performed IHC with the AM3 antibody on normal murine pancreas or pancreata that had developed PanIN lesions or PDAC. We observed EIIIB expression in the stroma of PanIN lesions and very strong EIIIB staining in the

PDAC stroma, whereas no EIIIB was detected in normal pancreas (Fig. 4*A*). These results indicated increasing inclusion/expression of FN containing EIIIB during PDAC progression in mice. Furthermore, IHC with NJB2-biotin on tissue sections of human PDAC samples showed that the nanobody binds to the EIIIB expressed in human PDAC stroma (Fig. 4*A*).

To test the binding of NJB2 to PDAC tumors in vivo, control and PDAC-bearing mice were injected via the tail vein with NJB2 sortagged with Alexa 647. Two hours after injection, mice were euthanized; pancreas and spleen were resected and imaged by two-photon microscopy. The nanobody bound to the ECM in PDAC tumors but not to ECM in the normal spleen (Fig. 4*B*), nor to the ECM of normal pancreas.

As a further test of in vivo binding, 2–8-mo-old KPC mice were injected via tail vein with ^{64}Cu-NJB2 and imaged with PET/CT 2 h later. Age-matched littermate controls with normal pancreas showed signals in the organs of elimination (kidney, bladder, liver, and intestine; Fig. 4 *C*, *i*, and Fig. 4*E*), whereas, in mice with PanINs, additional strong PET signals were evident in the region of the pancreas (Fig. 4 *C*, *ii* and *iii*, arrowheads, and *SI Appendix*, Fig. S6). In an independent experiment, ex vivo imaging of organs from PanIN-bearing mice confirmed that the source of the PET signal was the pancreas and not other surrounding organs such as the intestines (*SI Appendix*, Fig. S6). In a mouse with PDAC imaged with ^{64}Cu-NJB2 PET/CT, the nanobody bound specifically to two large pancreatic tumors (Fig. 4*C*, *iv*, "P" and "S"). The same mice were also imaged with ^{18}F-FDG for comparison (Fig. 4 *C*, *v*–*viii*). Although the large pancreatic tumors were clearly detected by ^{18}F-FDG (Fig. 4 *C*, *viii*, "P" and "S"), the PanIN lesions were not clearly visible with ^{18}F-FDG PET/CT imaging (Fig. 4 *C*, *vi* and *vii*).

The in vivo PET signals indicated a higher PET SUV in PDAC-bearing pancreas compared with pancreas that had PanIN lesions, as detected by ^{18}F-FDG and ^{64}Cu-NJB2 PET/CT (Fig. 4*D*). Signals from control mice could not be quantified because the anatomical resolution/definition of the normal pancreas did not allow designation of a region of interest for in vivo quantification. The pancreas-to-muscle ratios of PDAC-bearing pancreata were not significantly different between ^{64}Cu-NJB2 or ^{18}F-FDG imaging. However, in PanIN-bearing pancreata, the pancreas-to-muscle ratio was 4.5-fold higher in ^{64}Cu-NJB2 imaging compared with ^{18}F-FDG imaging (Fig. 4*D*, *Inset*).

Ex vivo biodistribution analysis showed 18-fold higher uptake of ^{64}Cu-NJB2 for PDAC and sevenfold higher uptake for PanIN compared with the pancreas of a control mouse (Fig. 4*E*). The tumor-to-blood ratios were 8.4 and 5.2 for pancreata with PDAC and PanINs, respectively. H&E staining of pancreas from the PDAC-bearing mouse imaged in Fig. 4 *C*, *iv*, showed that, in addition to a PDAC tumor ("P"), the pancreas of this mouse had also developed a large fibrosarcoma (Fig. 4*F*, *Right*, "S"), as sometimes occurs in the KPC model (37). Strong ECM staining following IHC with NJB2-biotin indicated high levels of EIIIB expression in both pancreatic tumors ("P" and "S"), but not in normal pancreas. H&E staining on PanIN-bearing pancreas showed regions that had progressed to different stages of PanIN (Fig. 4*F*, *Left*). EIIIB expression was observed in the stroma surrounding PanINs of different stages including early and late PanIN lesions but not in the "normal" regions of the pancreas (Fig. 4*F*, "N"). NJB2 can thus be used for noninvasive early detection and screening of PDAC and also for monitoring PDAC progression with high specificity and sensitivity.

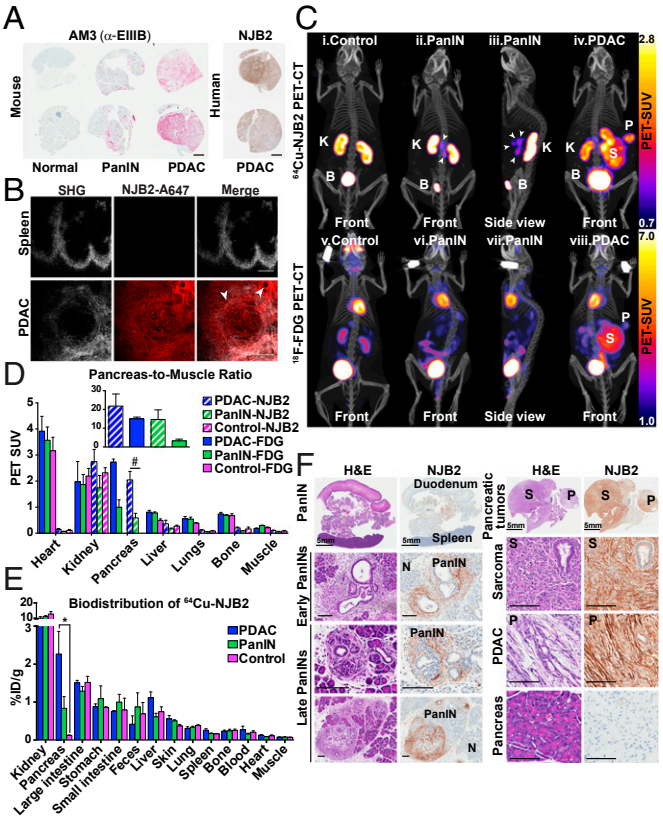

Fig. 4. NJB2 nanobody in early detection of pancreatic cancer. (*A*) Representative IHC images with AM3 and NJB2-biotin on tissues derived from mouse and human pancreas. Expression of EIIIB was absent in normal pancreas, whereas increasing expression of EIIIB was observed in the tumor stroma during PDAC progression. (Scale bars, 1 mm.) (*B*) Representative two-photon microscopy images of indicated organs resected from PDAC-bearing mice injected with NJB2-Alexa 647. Collagen distribution (second harmonic generation; *Left*), Alexa 647 signal (*Center*), and overlay of both channels (*Right*). NJB2-Alexa 647 bound to the ECM of a pancreas with advanced PDAC (*Lower*) but not to the ECM of spleen (from control or tumor-bearing mice; *Top*). (Scale bars, 100 μm.) (*C*) Control mice and KPC mice with PanINs and PDAC were imaged with ^{64}Cu-NJB2 PET/CT (*Top*) and ^{18}F-FDG PET/CT (*Bottom*). Representative PET/CT images of control mice (*i*), mice with PanIN (*ii* and *iii*), and mice with PDAC (*iv*) imaged with ^{64}Cu-NJB2, and control mice (*v*), mice with PanIN (*vi* and *vii*), and mice with PDAC (*viii*) imaged with ^{18}F-FDG PET/CT. Movies S8–S13 show 3D visualization (*SI Appendix*, Fig. S6). B, bladder; K, kidney. (*D*) Quantification of in vivo PET signals calculated as PET SUV for ^{18}F-FDG ("FDG") and ^{64}Cu-NJB2 ("NJB2"). In control, PanIN, and tumor-bearing mice, the PET SUV values were similar in various organs except the pancreas (#). (*Inset*) Pancreas-to-muscle ratio in ^{64}Cu-NJB2 and ^{18}F-FDG PET/CT were comparable for PDAC tumors (blue). However, ^{64}Cu-NJB2 had a 4.5 times higher pancreas-to-muscle ratio compared with ^{18}F-FDG for detection of PanIN lesions (green; $n = 3$ for all groups except PanIN-FDG, $n = 2$). (*E*) Ex vivo biodistribution of ^{64}Cu-NJB2, expressed as %ID/g (mean ± SE) in various organs, was similar except for pancreas, in which an 18-fold greater uptake was seen in PDAC and sevenfold higher uptake was seen in pancreata with PanINs ($n = 3$ for all groups). (*F*) Representative H&E staining and IHC of pancreata from PDAC-bearing and PanIN-bearing mice. (*F, Left*) In PanIN-bearing mice, NJB2-biotin bound to ECM surrounding PanIN lesions of different stages, including some early PanIN lesions. No binding was seen in the ECM of normal regions of this pancreas (marked as "N"). (*F, Right*) Pancreas of PDAC-bearing mouse (Fig. 4*C*, *iv*) had a sarcoma ("S") and an adenocarcinoma ("P"). IHC with NJB2-biotin showed strong staining in the ECM of both tumors. Normal pancreas was negative (*Bottom Right*). (Scale bars, 100 μm.)

Noninvasive Detection and Tracking of Pulmonary Fibrosis with ^{64}Cu-NJB2. Fibrosis is characterized by the excessive deposition of ECM containing FN. The expression of FN containing EIIIB is low or absent in normal tissues but high in sites of fibrosis (23). Bleomycin has been used widely to induce experimental lung fibrosis mimicking many aspects of clinical pulmonary fibrosis (39). Mice treated with a single intratracheal dose of bleomycin develop early histopathological features of interstitial pulmonary fibrosis 1 wk after administration (Fig. 5*C*). H&E staining 14 d after bleomycin administration indicated that fibrosis continued to progress, with increased deposition of ECM evident in fibrillar

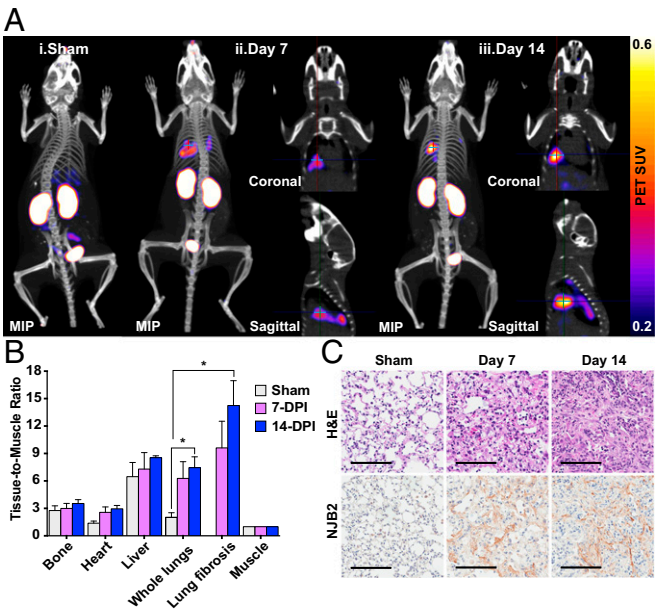

Fig. 5. NJB2 detects pulmonary fibrosis in a bleomycin-induced lung fibrosis model. (*A*) Pulmonary fibrosis was induced by a single intratracheal administration of 0.035U of bleomycin sulfate into C57BL/6 mice. Sham and bleomycin-treated mice (7 and 14 d after bleomycin administration) were imaged with ^{64}Cu-NJB2 PET/CT. Representative PET/CT images of mice that were sham-treated (*i*), 7 d after bleomycin treatment (*ii*), and 14 d after bleomycin treatment (*iii*). Fibrotic lesions were visible in mice at 7 and 14 d postadministration. The cross-hairs in the coronal and sagittal slices mark the locations of the fibrotic lesions within the lungs. Movies S14–S22 show 3D visualization (*SI Appendix*, Fig. S7*A*). MIP, maximum intensity projection. (*B*) The in vivo PET signals were quantified, and the TMR was significantly higher in bleomycin-treated mice at day 14 compared with sham controls (analyzed by two-tailed unpaired *t*-test). (*C*) Following ^{64}Cu-NJB2 PET/CT imaging, lungs were resected for histopathological analysis. Representative H&E images of lung sections indicated bleomycin-induced pulmonary fibrosis progression in mice at days 7 and 14 after administration (*SI Appendix*, Fig. S7*B*). No fibrosis was observed in sham-treated mice. (Scale bars, 100 μm.)

structures. Sham-treated mice did not show any histological features of fibrosis (Fig. 5*C*). Fibrosis induction in this model is heterogeneous, and not all lung lobes had the same extent of fibrosis (*SI Appendix*, Fig. S7*B*). IHC with NJB2-biotin showed that EIIIB expression in the fibrotic lungs was also heterogenous and had a "focal" appearance with more EIIIB expressed in some regions compared with others (*SI Appendix*, Fig. S7*B*). Whereas peak fibrotic response was observed by H&E staining 14 d after bleomycin administration, EIIIB expression was evident and abundant even 7 d after administration. This shows that NJB2 can detect early fibrosis (Fig. 5*C*, *Bottom*).

Bleomycin- and sham-treated mice were imaged with ^{64}Cu-NJB2 PET/CT. The nanobody bound to regions of fibrotic lung, showing distinct signals in the lungs at days 7 and 14 after bleomycin treatment (Fig. 5*A* and *SI Appendix*, Fig. S7*A*). The uptake of ^{64}Cu-NJB2 (measured in whole lungs and regions of lung fibrosis) showed an increase at 7 and 14 d after bleomycin administration compared with sham-treated mice as observed from the TMR of the PET SUV (Fig. 5*B*). Although no significant differences were observed in the TMR from other organs, at day 14, the TMR was significantly higher for whole lungs and lung fibrosis region than for sham-treated controls. We conclude that ^{64}Cu-NJB2 detects early pulmonary fibrosis noninvasively with good specificity and signal-to-noise ratio.

^{64}Cu–NJB2 Detects Tumor Progression in Breast Cancer. Noninvasive monitoring of disease progression (such as in response to therapy) is an important application of in vivo imaging. To assess whether ^{64}Cu-NJB2 could be a useful tool in this application, we chose the MMTV-PyMT model of breast cancer progression, in which mice develop spontaneous autochthonous tumors. This model recapitulates many aspects of human breast cancer progression (40). Tumor progression occurs via four distinct stages: hyperplasia (4–6 wk of age), premalignant adenoma (8–9 wk of age), and early carcinoma (malignant transition at 8–12 wk of age), which then progresses to advanced carcinoma (40).

We used longitudinal immuno-PET/CT imaging to monitor tumor progression. MMTV-PyMT females ($n = 7$) were imaged with ^{64}Cu-NJB2 PET/CT from 6 wk to 13 wk. PET signals from mammary fat pad tumors were evident in 10-wk-old mice (Fig. 6*A*). As tumor growth progressed from week 10 to week 13, PET signals were observed from multiple macroscopic tumor nodules in all mice. Progression of individual tumors was then monitored. Tumors from 13-wk-old mice had a significantly higher in vivo PET SUV signal compared with signals from mammary fat pads of control FVB mice (Fig. 6*B*). Immediately after imaging, mice were euthanized and organs were resected for biodistribution analysis. A 2.2-fold higher uptake of ^{64}Cu-NJB2 was seen in the tumors of 13-wk-old mice compared with fat pads of the FVB control (Fig. 6*C*, #).

Histopathological analysis of tumors excised from 13-wk-old mice imaged with ^{64}Cu-NJB2 showed EIIIB expression in some regions (but not all) of the tumor capsules (Fig. 6*D*, arrowhead). Little to no EIIIB expression was seen in the tumor stroma. Overall expression of EIIIB in this model was lower than in the LM2 and PDAC models. We did not observe any signal from the control (no NJB2; Fig. 6*D*). The lower expression of EIIIB in this model explains the lower tumor-to-blood ratio of 3.9 seen in ^{64}Cu-NJB2 PET/CT, compared with 16.9 in LM2 breast cancer and 8.4 in the PDAC model. NJB2 can thus be used to target and monitor tumor progression even in mouse models that express low levels of EIIIB.

^{64}Cu–NJB2 Detects FN-EIIIB in Mouse Cartilage. Although EIIIB-containing FN is largely absent from normal adult tissue, some evidence suggests that it is expressed in normal cartilaginous tissue (41, 42). To investigate whether NJB2 can detect EIIIB in mouse cartilage, EIIIB-KO mice were imaged with ^{64}Cu-NJB2 PET/CT. PET/CT images of the EIIIB-KO mice were compared with images of mice with different genetic backgrounds that are WT for EIIIB. In the NSG background (control of Fig. 3) and C57BL/6J background (control of Fig. 4), a clear signal could be detected, albeit at much reduced levels, from multiple bone joints, including the shoulder joint (Fig. 6*E*, white arrowhead) and mouse nose/snout (Fig. 6*E*, green arrowhead), but not in the EIIIB-KO mice. These results highlight the sensitivity of the NJB2 nanobody in detecting the lower levels of EIIIB found in cartilage by immuno-PET and genetically validate its specificity.

^{64}Cu–NJB2 Detects Tumors and Metastases in Syngeneic Models of Melanoma and TNBC. We next explored whether the NJB2 nanobody can target and detect tumors and metastases in immunocompetent syngeneic models of melanoma (B16F10 in C57BL/6) and breast cancer (4T1 in BALB/c). The 4T1 tumors are a model of TNBC, which can spontaneously metastasize to distant sites, including lung, liver, and LNs. Mice bearing B16F10 or 4T1-Luc-ZsGreen primary tumors or pulmonary metastases were injected via the tail vein with NJB2-Texas Red and NJB2-A647, respectively. Mice were euthanized 2 h later, and tumors and lungs were excised for confocal microscopy. In primary tumors and lung metastases, the nanobody bound to the ECM surrounding ZsGreen tumor cells (Fig. 7*A*). Representative images of 4T1-derived primary tumor and B16F10-derived lung metastases are shown in Fig. 7*A*.

Mice bearing primary tumors or pulmonary metastases were further imaged with ^{64}Cu-NJB2 PET/CT, which detected the tumors and lung metastases with high specificity in both models (Fig. 7 *B* and *C*). Nonspecific PET signals were absent from the corresponding control mice. Postmortem histology confirmed

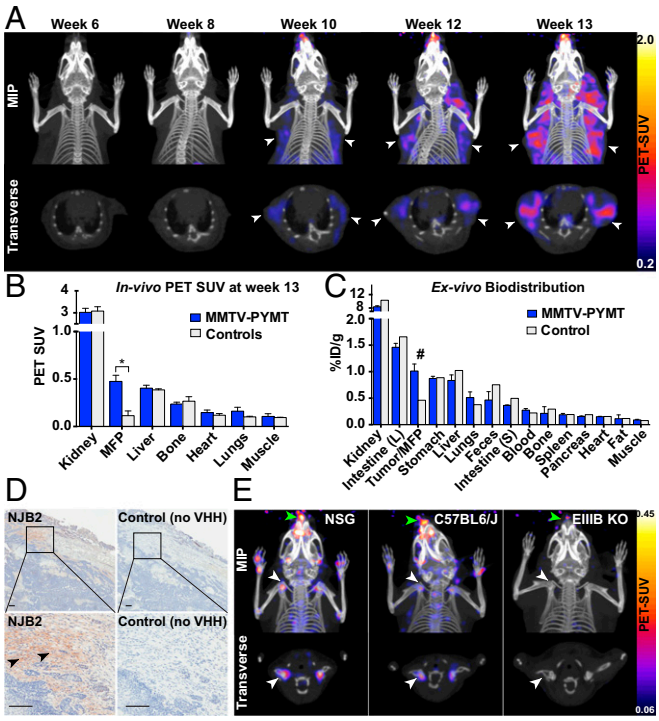

Fig. 6. Serial PET/CT imaging to track tumor progression in MMTV-PyMT mice. (*A*) Representative PET/CT images of the upper body of MMTV-PyMT mice ($n = 7$) imaged by ^{64}Cu-NJB2 PET/CT at the ages of 6, 8, 10, 12, and 13 wk. Clear PET/CT signals from mammary fat pad tumors were visible from week 10 and onward (arrows). Tumor progression in multiple mammary tumors was evident in all mice. Movies S23–S27 show 3D visualizations. (*B*) The in vivo PET signals (quantified as PET SUV) from the mammary fat pads (MFP)/tumors were significantly higher in the 13-wk-old MMTV-PyMT mice compared with controls. The signals from other organs were comparable. Data were analyzed by two-tailed unpaired *t*-test ($n = 3$ for PYMT mice, $n = 2$ for controls). (*C*) Ex vivo biodistribution of ^{64}Cu-NJB2 expressed as %ID/g (mean ± SE) in various organs of 13-wk-old MMTV-PyMT mice ($n = 3$ for PYMT mice, $n = 1$ for controls). (*D*) Representative IHC images with NJB2-biotin and no-VHH control in tumors derived from 13-wk-old MMTV-PyMT mice. EIIIB staining was observed in the tumor capsule (arrowhead), with little or no signal from tumor stroma. (Scale bars, 100 μm.) (*E*) EIIIB-KO mice were imaged with ^{64}Cu-NJB2 PET/CT. Note that lower PET SUV scales compared with Figs. 3 and 4 were used to allow visualization of lower signals from cartilage. Comparison of representative images of PET/CT data [maximum-intensity projections (MIPs) of all slices and transverse sections] acquired from the EIIIB-KO mice with control mice WT for EIIIB expression that were imaged in previous experiments (Figs. 3 and 4). In control mice [NSG background (Fig. 3*A*) and C57BL/6J background (Fig. 4*C*)], clear signals were visible from cartilaginous tissue, such as shoulder joints (white arrow) and the nose/snout (green arrow). These signals were not detected in the EIIIB-KO mice ($n = 2$).

EIIIB expression in the primary tumors and lung metastases in both tumor types (Fig. 7 *D* and *E*). In 4T1 primary tumors, negligible EIIIB staining was detected in the tumor core that consisted of necrotic/dead tissue compared with tumor regions with live cells. NJB2 staining was also seen in the ECM of 4T1-derived lung metastases but not in liver samples from mice bearing tumors or lung metastases. In the B16F10 s.c. tumors, EIIIB staining was seen largely in the tumor capsule (Fig. 7*E*), consistent with the PET signal observed in this tumor. EIIIB expression was also validated in the B16F10-derived lung metastases (Fig. 7*E*).

FN-EIIIB Is Widely Expressed in Metastases Derived from Multiple Cancer Types. Having demonstrated that the nanobody can detect small metastases in a TNBC model, which remains technically challenging with conventional imaging methods, we wished to assess how broadly NJB2 can be used for the detection and targeting of metastases. To investigate the expression of EIIIB in metastases from patients, we used NJB2-biotin to stain a multiorgan tissue array of samples from various metastatic sites derived from 104 patients (Fig. 8*A*). Tissues were scored for EIIIB signal in the ECM and ∼44% of patients showed expression of EIIIB at metastatic sites (Fig. 8*B*). These metastases to multiple organs (21 distinct sites) were derived from 17 different primary sites, including rectum, pancreas, lung, ovary, stomach, and thyroid, among others (Fig. 8 *C* and *D*). Among the EIIIB-positive biopsies, ∼32% were metastases to the LNs at the metastatic sites (Fig. 8*D*, blue). This wide expression of EIIIB at metastatic sites in multiple organs and derived from multiple types of primary tumors further broadens the potential applications of NJB2-based imaging and therapeutic applications. As tumors can be heterogeneous in their expression of EIIIB, small biopsies from EIIIB-positive tumors may score as negative in these arrays. This may not be the case for PET imaging, in which the entire tumor is imaged.

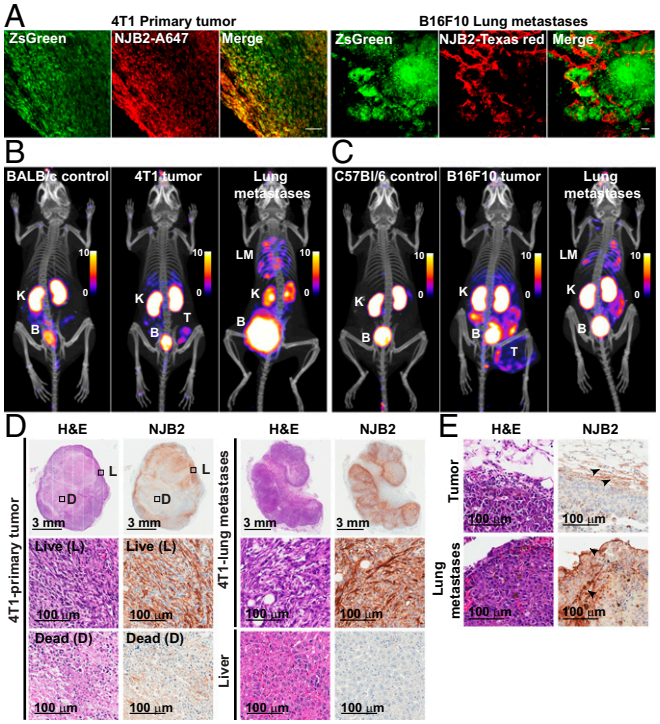

Fig. 7. ^{64}Cu–NJB2 detects tumors and metastases in syngeneic models of melanoma and TNBC. (*A*) 4T1-Luc-ZsGreen cells (1×10^6) were injected into mammary fat pads of BALB/c mice. After 2.5 wk, mice were injected i.v. with NJB2-Alexa 647 and euthanized 2 h after injection, and excised tumors were imaged by using confocal microscopy (*Left*). Albino C57BL/6 mice were injected via the tail vein with 0.5×10^6 B16F10-Luc-ZsGreen cells. Mice were injected i.v. with NJB2-Texas Red 2.5 wk after tumor induction, and resected lungs were imaged with confocal microscopy (*Right*). (*B* and *C*) BALB/c mice were injected in the mammary fat pad or via the tail vein with 0.25×10^6 4T1-Luc-ZsGreen cells. Albino C57BL/6 mice were injected s.c. (0.5×10^6) or via the tail vein (0.2×10^6) with B16F10-Luc-ZsGreen cells. After 3 wk, mice were imaged with ^{64}Cu-NJB2 PET/CT. Representative PET/CT images show PET signals from the primary tumor (marked as "T"), lung metastases ("LM"), kidneys ("K"), and bladder ("B"); PET scale bars have arbitrary units (Movies S28–S33). (*D and E*) Representative H&E images and IHC with NJB2-biotin on tissue sections from tumors and lung metastases derived from 4T1-Luc-ZsGreen cells (*D*) and B16F10-Luc-ZsGreen cells (*E*). The 4T1 primary tumors had little EIIIB staining in the necrotic center ("D") compared with other regions with live cells ("L") (*D*). Abundant EIIIB expression was observed in the 4T1-derived lung metastases (*D*, *Right*). EIIIB expression was confirmed in B16F10-derived tumors and metastases (*E*).

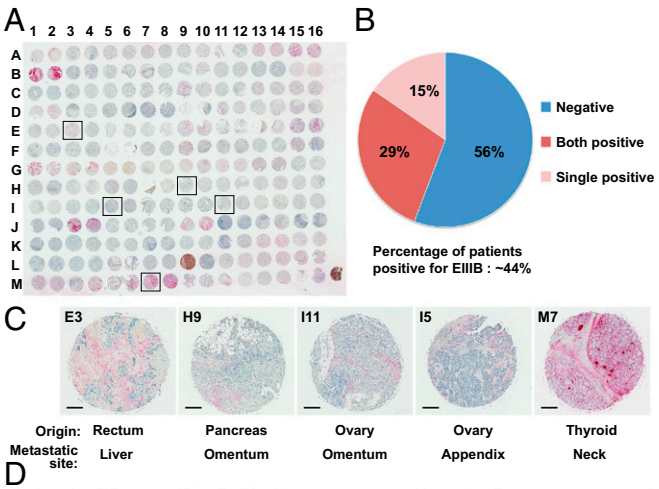

D

Primary site	Both positive	Single positive	Metastatic site(s)		
Thyroid	4	1	Neck (9)		
Endometrium	3		Vaginal wall (2)	Abdominal cavity (2)	Pelvic cavity (2)
Lung	3		Left frontal lobe (4)	Mediastinum (2)	
Ovary	2	2	Omentum (1)	Peritoneum (3)	Appendix (2)
Cervix	2	1	Colon (2)	Abdominal wall (2)	Pelvic cavity (1)
Bladder	2	2	Penis (1)	Back (2)	Pelvic cavity (3)
Kidney	2		Adrenal gland (2)	Renal Hilum (2)	
Oesophagus	2		Around oesophagus (2)	Mediastinum (2)	
Rectum	2	2	Ovary (3)	Liver (3)	
Duodenum	2		Mesentry (2)	Omentum (2)	
Stomach	2	1	Omentum (4)	Cardia (1)	
Penis	1		Groin (2)		
Larynx	1	1	Neck (3)		
Colon	1	1	Mesentry (2)	Liver (1)	
Skin	1		Occipital lobe (2)		
Pancreas		4	Omentum (2+2)		
Vulva		1	Groin (1)		

Fig. 8. FN-EIIIB expression in a multiorgan patient metastatic tissue array. (*A*) IHC with NJB2-biotin on a metastatic tissue array with biopsy samples from 104 patients (two biopsies per patient) derived from multiple organs. (*B*) Nearly 44% of the patients had metastases that were positive for stromal EIIIB. This includes patients in whom both biopsies were positive (29%) and those in whom a single biopsy was positive (15%). (*C*) Representative examples of metastases derived from different primary tumor types to distinct metastatic sites are highlighted (E3, H9, I11, I5, M7). (Scale bars, 200 μm.) (*D*) Summary table indicating the primary and metastatic sites of patient biopsies that were positive for stromal EIIIB. The numbers in the parentheses indicate biopsies positive at each site, and the numbers indicated in blue are metastases present at the LNs of the metastatic sites.

Discussion

To exploit the ECM as an imaging and therapeutic target, we made nanobody libraries against ECM proteins associated with tumor progression and metastases. We immunized alpacas with a mixture of ECM proteins (including specific domains and peptides) or with ECM-enriched preparations derived from patient metastasis samples. We generated four separate nanobody libraries, which likely contain within them sequences of VHHs that bind many diverse components of this disease-associated ECM. This approach circumvents the need to express and purify ECM proteins, many of which are large and insoluble, and should facilitate further exploration of the ECM, hampered thus far by limited availability of high-quality ECM-specific antibodies (27). These libraries can be a valuable resource for the selection of novel nanobodies against a diverse set of ECM and ECM-associated antigens involved in disease. The nanobodies are readily expressed, equipped with sortase tags (30) that facilitate rapid and efficient addition of diverse imaging and therapeutic cargoes.

To demonstrate the utility of such ECM-specific nanobodies in imaging and targeting tumors and metastases, we describe a high-affinity nanobody, NJB2, specific for the EIIIB domain of FN. To confirm that this nanobody was selectively and specifically recruited to sites of tumors and metastases in vivo, we took advantage of sortase-mediated tagging of nanobodies with diverse probes to enable several imaging methods: conventional IHC, two-photon immunofluorescence, and noninvasive immuno-PET/CT–based imaging.

Although widely used in the clinic for noninvasive diagnostic imaging of cancer patients, ^{18}F-FDG PET imaging has several limitations in cancer detection (34). Uptake is observed at sites of metabolic activity other than tumors and metastases, such as sites of inflammation and infection, and in lymphoid tissues, muscle, and brown fat. PET with ^{18}F-FDG is also less effective in detecting desmoplastic and hypocellular tumors and lesions that have low metabolic activity (34). We tested the nanobody in three different mouse models of metastatic breast cancer and in PDAC, melanoma, and pulmonary fibroses. In all these diseases, early therapeutic intervention aided by early detection can be beneficial and often curative (1). In the LM2 TNBC model, PET/CT using ^{64}Cu-NJB2 detected orthotopic tumors and metastases to multiple organs including lung, liver, and LNs with high selectivity and excellent signal-to-noise ratios. Compared with ^{18}F-FDG PET/CT imaging, ^{64}Cu-NJB2 PET/CT imaging resulted in higher clarity and significantly higher TMR for primary tumors and metastatic lesions seeded from orthotopic tumors. This model reflects late-stage clinical disease when patients present with distant organ metastases. The immuno-PET signals correlated well with the expression levels of EIIIB in tumors and metastases. PET/CT with ^{64}Cu-NJB2 enabled evaluation of the exact location and size of the metastatic lesions and detected metastases as small as ∼2.5 mm. This sensitivity of lesion detection can likely be increased with technical adjustments, such as longer scan times and the conjugation of more efficient PET emitters such as ^{18}F conjugated to NJB2.

PDAC is a progressive desmoplastic disease with poor prognosis. Patients usually present with advanced metastatic disease (43). Late detection is associated with high mortality rates, and early detection remains a clinical challenge. Currently, there are no noninvasive methods for early detection of PDAC. Clinical screening methods rely on anatomical data such as CT and MRI for diagnosis. Therefore, there is an urgent need for sensitive and specific tools for early detection of PDAC (43). We show that EIIIB is expressed around PanINs, an early stage that precedes PDAC, and that its expression increases with PDAC progression in mouse models and human patient samples (Fig. 4*A*). To the best of our knowledge, this is the first demonstration of EIIIB expression in the ECM of PanINs. Immuno-PET/CT imaging with ^{64}Cu-NJB2 detected early and late stages of PDAC, and early stages were detected far more effectively than with ^{18}F-FDG. With further testing, the NJB2 nanobody may be developed into an excellent tool for early detection, staging, and potential therapeutic intervention for PDAC in humans as well, given the sequence identity of EIIIB in human and mouse.

Pulmonary fibrosis is a group of diseases with varied etiology (44). It includes idiopathic pulmonary fibrosis, a progressive and fatal disease in which patients remain asymptomatic until the late stage of disease (45). There is no treatment to prevent or reverse progression. Diagnosis is based on high-resolution CT, often followed by biopsy to confirm disease (45). In the commonly used bleomycin-induced lung fibrosis model, we demonstrated that ^{64}Cu-NJB2 PET/CT detected an early fibrotic response. Fibrotic lesions were detected as early as 7 d after administration of bleomycin, a stage that precedes the complete fibrotic response observed at day 14. Imaging with ^{64}Cu-NJB2 may be used in combination with current clinical imaging methods for early detection and for monitoring response to therapy. This approach could be easily extended to other fibrotic disorders.

The identification of PanIN lesions and early fibroses indicates that NJB2 can detect early stages of ECM deposition and raises the possibility that NJB2 can be used in early detection and intervention in multiple kinds of disorders characterized by ECM deposition. Imaging of tumor progression in the MMTV-PyMT model showed that NJB2 can be used as a preclinical tool to monitor tumor progression. Real-time imaging of the response

to treatment may assist in drug discovery (46). The detection of MMTV-PyMT tumors, which express relatively low levels of EIIIB, further demonstrates the sensitivity of the method. Despite repeated administration of NJB2, we saw no obvious signs of an immune response in any of the PyMT mice. Sequence conservation of the EIIIB domain in multiple species including human, rat, and mouse allows wider testing of NJB2 in preclinical models and subsequent clinical translation without the need for the development of a separate human-specific antibody.

Although various strategies have been used to image and target FN-EIIIB in tumors (12, 13, 47, 48), many of these are based on the widely tested recombinant scFv L19. Its slow clearance from the circulation results in low tumor-to-blood ratios even 6 h after injection (49, 50). Noninvasive diagnostic imaging requires agents that clear rapidly, with acceptable specificity for target sites and better signal-to-noise ratios. Nanobodies like NJB2 meet these benchmarks (31), with excellent signal-to-noise ratio within 2 h after injection as demonstrated in various mouse models. This is a significant advantage not only for noninvasive diagnostic imaging, but also for therapeutic applications in which fast blood clearance may result in reduced systemic toxicities.

Aspects that remain to be explored are the sensitivity of this nanobody in detecting small metastases (<2.5 mm) in different models of cancer. Although the nanobody may aid in defining the spatial location of disease tissue, one caveat of this approach may be the inability to distinguish between fibrotic and cancer tissues. EIIIB is also expressed during wound healing and angiogenesis. Additional imaging methods such as ^{18}F-FDG PET/CT or post-imaging tissue biopsies may be needed to ascertain the nature of disease, such as to distinguish lung cancer from lung fibrosis.

This study has focused on using noninvasive imaging to validate the in vivo specificity of the NJB2 nanobody for disease ECM. An exciting future direction will be to use ECM-specific nanobodies as vehicles to deliver therapeutic cargo including immunomodulators, α-emitting isotopes, drugs, and nanoparticles. High and sustained target retention is desirable to reduce frequency of dosing and to achieve sustained local release. The observations that NJB2 remains bound to primary tumors even 24 h after administration (Fig. 2*C*) is an encouraging sign for its future use in such applications. Other targeted therapies often suffer from systemic toxicities as a result of wider expression of the proteins targeted. Therapies such as HER2-specific antibodies for breast and ovarian cancer or anti-CD20 for lymphoid tumors are based on tumor-specific antigens and are restricted to cancer type. We speculate that the selective expression of the EIIIB domain at sites of disease, its wide expression in various tumor types and metastases demonstrated by our assessment of EIIIB expression in a multicancer human tissue array (Fig. 8), as well as specific binding of NJB2 to its target protein will allow a significant improvement over other targeted approaches currently available. Accumulation of nanobody-bound therapeutic cargo in the ECM of disease sites should increase the therapeutic index of systemically toxic drugs and reduce vascular leak syndrome. The low immunogenicity of the nanobodies (17, 18) should make any targeted agent poorly visible to the immune system, thereby reducing systemic toxicities. An example of such an application is presented in an accompanying paper (51), which describes incorporation of the NJB2 nanobody into CAR T cells to enhance their antitumor activity. The imaging of the EIIIB-KO mice and the detection of normal mouse cartilage by NJB2 (Fig. 6*E*) are a reminder that the design of therapeutic strategies targeting EIIIB must also consider potential side effects on the few tissues expressing EIIIB such as cartilage, female reproductive tissues, and other sites of physiological angiogenesis (52).

In summary, we have developed nanobody libraries that contain functional binders against ECM proteins expressed at sites of several diseases. As an example of the utility of these reagents, we validated a high-affinity nanobody, NJB2, specific for the FN-EIIIB splice variant expressed in the ECM of tumors, metastases, and other diseases characterized by ECM deposition. By using immuno-PET/CT, we showed that the ^{64}Cu-NJB2 nanobody readily detects primary tumors and metastases in multiple models of cancer. The high sensitivity of the nanobody allowed detection of discrete metastases in a breast cancer model and early lesions in PDAC progression, both of which were not clearly detected by ^{18}F-FDG PET/CT, the standard imaging tool in the clinic. We propose the NJB2 nanobody as a powerful tool for noninvasive detection and targeting of tumors, metastatic lesions, and fibroses.

Materials and Methods

C-Terminal Sortase Tagging with Biotin, Texas Red, or Alexa Fluor 647. *Staphylococcus aureus* sortase A (pentamutant variant, "5M-SrtA") purification and sortase-mediated tagging was done as previously described (30). Briefly, pentamutant SrtA (5 μM) was incubated with purified VHH (100 μM) and nucleophile (GGGK-Biotin/GGGC-Texas Red/GGGC-Alexa 647, 500 μM) in sortase buffer containing 50 mM Tris·HCl, pH 7.5, 150 mM NaCl, 10 mM $CaCl_2$ for 3 h at 4 °C. To remove unreacted sortase and VHH, the reaction was incubated with Ni-NTA beads with agitation for 5 min at 25 °C followed by centrifugation. The tagged VHH was purified by size-exclusion chromatography in PBS solution or Tris·HCl (50 mM, pH 7.5) and stored with 5% glycerol at −20 °C.

Synthesis of ^{64}Cu-NJB2 and ^{64}Cu-96G3M. $(Gly)_3$-Cys-NOTA was synthesized as described before (31). Briefly, maleimide-NOTA (Macrocyclics) was dissolved in 0.1 M $NaHCO_3$, pH 8.3. The tetrapeptide GGGC was added at room temperature for 30 min until LC-MS analysis indicated a near-complete conversion to the product. The product was purified by reversed-phase HPLC on a semi-preparative column (Phenomenex, C18 column, Gemini, 5 μm, 10 Å × 250 mm) at a flow rate of 4.0 mL/min (solvent A, 0.1% TFA in H_2O; solvent B, 0.1% TFA in CH_3CN). The desired product eluted from 15% to 20% (vol/vol) solvent B. Fractions containing pure product were collected and lyophilized. LC-MS calculated for $C_{27}H_{45}N_{10}O_{11}S$ [M+H]+ was 717.298 (found = 717.305). NJB2 and 96G3M were site-specifically labeled with GGG-NOTA by using sortagging. ^{64}Cu–VHHs were synthesized and characterized as reported previously (31). In brief, a typical reaction was performed in a 1.5-mL centrifuge tube loaded with VHH-NOTA (400 μL, ∼12–15 μM in PBS solution) and $^{64}CuCl_2$ (usually in the range of 30–40 MBq) in 200 mM NH_4OAc buffer (100 μL, pH 6.5). The tube was sealed and shaken at room temperature for 20 min. At this time, the mixture was loaded onto a PD-10 size-exclusion cartridge, and elution with 1× PBS solution provided radiolabeled ^{64}Cu-VHH in >90% decay-corrected radiochemical yield.

PET/CT Imaging. PET/CT imaging with ^{64}Cu-NJB2, ^{64}Cu-96G3M, and ^{18}F-FDG was performed by using a G8 PET/CT preclinical, small-animal scanner (PerkinElmer). The system has >14% PET sensitivity and a spatial resolution of 1.4 mm. Mice were anesthetized with isoflurane (2% mixed in oxygen) before injection of PET probes and during PET scanning. For ^{18}F-FDG imaging, mice were fasted for 10–12 h before imaging. Mice were injected via the lateral tail vein with 100 μCi of radiotracer, ^{64}Cu-NJB2 (∼5 μg) or ^{18}F-FDG, in 100 μL of sterile PBS solution. For immuno-PET/CT imaging with ^{64}Cu-NJB2/^{64}Cu-96G3M, mice were allowed to wake up after probe injection and imaged 120 min after probe uptake. For ^{18}F-FDG imaging, mice were kept unconscious under isoflurane (2% mixed in oxygen) for 90 min to prevent tracer uptake in muscles. The body temperature of unconscious mice was maintained by using controlled heating pads. Mice were imaged with a static PET emission scan for 10 min followed by a 1.5-min CT scan for anatomical reference. The images were reconstructed by using the manufacturer's automatic image reconstruction software (MLEM 3D with 60 iterations).

Biodistribution Analysis of ^{64}Cu-Labeled NJB2. Mice were injected via tail vein with 108 ± 11 μCi of ^{64}Cu-NJB2 or 100 ± 3 μCi of ^{64}Cu-96G3M in 100 μL of sterile PBS solution. Mice were euthanized after PET/CT imaging, i.e., at 150 min after injection, and blood was immediately harvested by cardiac puncture. The mice were perfused with PBS solution (20 mL), different tissues were dissected and weighed, and tissue radioactivity was measured with a gamma-counter (2480 Wizard^2; PerkinElmer). Counts were decay- and background-corrected, and ^{64}Cu-NJB2 uptake was expressed as %ID/g for each tissue.

SI Appendix, Materials and Methods, provides details about nanobody methods, cell culture, histology, microscopy, PET/CT data analysis, and animal models.

ACKNOWLEDGMENTS. We thank Dr. Kenneth Tanabe and Dr. Saraswati Sukumar for patient metastases samples; Dr. Stephen R. Purdy for Alpaca immunizations; Christina Martone for technical assistance; Yushu Joy Xie for critical reading of the manuscript; Allison Lau for mice; Noor Momin for help

with FPLC; and Meghana Pandya, Jeff Wykoff, the histology core, and Dr. Roderick Bronson (Swanson Biotechnology Center, Koch Institute) for technical assistance. This work was supported by a Mazumdar–Shaw International Oncology Fellowship (to N.J.); a Massachusetts Institute of Technology Ludwig Center for Molecular Oncology Research postdoctoral fellowship (to C.T. and S.R.); the Howard Hughes Medical Institute, of which R.O.H. is an investigator; Department of Defense Breast Cancer Research Program Investigator Award W81XWH-14–1-0240 (to R.O.H.); National Cancer Institute Grant P30CA14051-45S1 (to R.O.H.); and a research grant from the Lustgarten Foundation, Inc. (to H.L.P.). C.T. was a Sherry and Alan Leventhal Family Fellow of the Damon Runyon Cancer Research Foundation. M.R. is an American Cancer Society Fellow.

1. Etzioni R, et al. (2003) The case for early detection. *Nat Rev Cancer* 3:243–252.
2. Steeg PS (2016) Targeting metastasis. *Nat Rev Cancer* 16:201–218.
3. Hynes RO (2009) The extracellular matrix: Not just pretty fibrils. *Science* 326:1216–1219.
4. Aoudjit F, Vuori K (2012) Integrin signaling in cancer cell survival and chemoresistance. *Chemother Res Pract* 2012:283181.
5. Correia AL, Bissell MJ (2012) The tumor microenvironment is a dominant force in multidrug resistance. *Drug Resist Updat* 15:39–49.
6. Astrof S, Hynes RO (2009) Fibronectins in vascular morphogenesis. *Angiogenesis* 12:165–175.
7. Bonnans C, Chou J, Werb Z (2014) Remodelling the extracellular matrix in development and disease. *Nat Rev Mol Cell Biol* 15:786–801.
8. Naba A, et al. (2014) Extracellular matrix signatures of human primary metastatic colon cancers and their metastases to liver. *BMC Cancer* 14:518.
9. Naba A, Clauser KR, Lamar JM, Carr SA, Hynes RO (2014) Extracellular matrix signatures of human mammary carcinoma identify novel metastasis promoters. *eLife* 3: e01308.
10. Gocheva V, et al. (2017) Quantitative proteomics identify Tenascin-C as a promoter of lung cancer progression and contributor to a signature prognostic of patient survival. *Proc Natl Acad Sci USA* 114:E5625–E5634.
11. Housman G, et al. (2014) Drug resistance in cancer: An overview. *Cancers (Basel)* 6: 1769–1792.
12. Kumra H, Reinhardt DP (2016) Fibronectin-targeted drug delivery in cancer. *Adv Drug Deliv Rev* 97:101–110.
13. Kaspar M, Zardi L, Neri D (2006) Fibronectin as target for tumor therapy. *Int J Cancer* 118:1331–1339.
14. Cox TR, Erler JT (2011) Remodeling and homeostasis of the extracellular matrix: Implications for fibrotic diseases and cancer. *Dis Model Mech* 4:165–178.
15. Karsdal MA, et al. (2013) Extracellular matrix remodeling: The common denominator in connective tissue diseases. Possibilities for evaluation and current understanding of the matrix as more than a passive architecture, but a key player in tissue failure. *Assay Drug Dev Technol* 11:70–92.
16. Yuzhalin AE, Urbonas T, Silva MA, Muschel RJ, Gordon-Weeks AN (2018) A core matrisome gene signature predicts cancer outcome. *Br J Cancer* 118:435–440.
17. Muyldermans S (2013) Nanobodies: Natural single-domain antibodies. *Annu Rev Biochem* 82:775–797.
18. Ingram JR, Schmidt FI, Ploegh HL (2018) Exploiting nanobodies' singular traits. *Annu Rev Immunol* 36:695–715.
19. Schwarzbauer JE, Patel RS, Fonda D, Hynes RO (1987) Multiple sites of alternative splicing of the rat fibronectin gene transcript. *EMBO J* 6:2573–2580.
20. Neri D, Bicknell R (2005) Tumour vascular targeting. *Nat Rev Cancer* 5:436–446.
21. Astrof S, et al. (2004) Direct test of potential roles of EIIIA and EIIIB alternatively spliced segments of fibronectin in physiological and tumor angiogenesis. *Mol Cell Biol* 24:8662–8670.
22. Bergmeier W, Hynes RO (2012) Extracellular matrix proteins in hemostasis and thrombosis. *Cold Spring Harb Perspect Biol* 4:a005132.
23. To WS, Midwood KS (2011) Plasma and cellular fibronectin: Distinct and independent functions during tissue repair. *Fibrogenesis Tissue Repair* 4:21.
24. Murphy PA, Hynes RO (2014) Alternative splicing of endothelial fibronectin is induced by disturbed hemodynamics and protects against hemorrhage of the vessel wall. *Arterioscler Thromb Vasc Biol* 34:2042–2050.
25. Schwarzbauer JE, DeSimone DW (2011) Fibronectins, their fibrillogenesis, and in vivo functions. *Cold Spring Harb Perspect Biol* 3:a005041.
26. Hynes RO (1990) *Fibronectins* (Springer-Verlag, New York).
27. Rickelt S, Hynes RO (2018) Antibodies and methods for immunohistochemistry of extracellular matrix proteins. *Matrix Biol* 71–72:10–27.
28. Bloom L, Ingham KC, Hynes RO (1999) Fibronectin regulates assembly of actin filaments and focal contacts in cultured cells via the heparin-binding site in repeat III13. *Mol Biol Cell* 10:1521–1536.
29. Peters JH, Trevithick JE, Johnson P, Hynes RO (1995) Expression of the alternatively spliced EIIIB segment of fibronectin. *Cell Adhes Commun* 3:67–89.
30. Guimaraes CP, et al. (2013) Site-specific C-terminal and internal loop labeling of proteins using sortase-mediated reactions. *Nat Protoc* 8:1787–1799.
31. Rashidian M, et al. (2015) Noninvasive imaging of immune responses. *Proc Natl Acad Sci USA* 112:6146–6151.
32. Anderson CJ, Ferdani R (2009) Copper-64 radiopharmaceuticals for PET imaging of cancer: Advances in preclinical and clinical research. *Cancer Biother Radiopharm* 24:379–393.
33. Sockolosky JT, et al. (2016) Durable antitumor responses to CD47 blockade require adaptive immune stimulation. *Proc Natl Acad Sci USA* 113:E2646–E2654.
34. Zhu A, Lee D, Shim H (2011) Metabolic positron emission tomography imaging in cancer detection and therapy response. *Semin Oncol* 38:55–69.
35. Feig C, et al. (2012) The pancreas cancer microenvironment. *Clin Cancer Res* 18: 4266–4276.
36. Yachida S, et al. (2010) Distant metastasis occurs late during the genetic evolution of pancreatic cancer. *Nature* 467:1114–1117.
37. Hingorani SR, et al. (2005) Trp53R172H and KrasG12D cooperate to promote chromosomal instability and widely metastatic pancreatic ductal adenocarcinoma in mice. *Cancer Cell* 7:469–483.
38. Westphalen CB, Olive KP (2012) Genetically engineered mouse models of pancreatic cancer. *Cancer J* 18:502–510.
39. Moeller A, Ask K, Warburton D, Gauldie J, Kolb M (2008) The bleomycin animal model: A useful tool to investigate treatment options for idiopathic pulmonary fibrosis? *Int J Biochem Cell Biol* 40:362–382.
40. Lin EY, et al. (2003) Progression to malignancy in the polyoma middle T oncoprotein mouse breast cancer model provides a reliable model for human diseases. *Am J Pathol* 163:2113–2126.
41. Peters JH, Chen GE, Hynes RO (1996) Fibronectin isoform distribution in the mouse. II. Differential distribution of the alternatively spliced EIIIB, EIIIA, and V segments in the adult mouse. *Cell Adhes Commun* 4:127–148.
42. Scanzello CR, et al. (2015) Fibronectin splice variation in human knee cartilage, meniscus and synovial membrane: Observations in osteoarthritic knee. *J Orthop Res* 33: 556–562.
43. Chari ST, et al. (2015) Early detection of sporadic pancreatic cancer: Summative review. *Pancreas* 44:693–712.
44. Wilson MS, Wynn TA (2009) Pulmonary fibrosis: Pathogenesis, etiology and regulation. *Mucosal Immunol* 2:103–121.
45. Ley B, Collard HR, King TE, Jr (2011) Clinical course and prediction of survival in idiopathic pulmonary fibrosis. *Am J Respir Crit Care Med* 183:431–440.
46. Weissleder R (2006) Molecular imaging in cancer. *Science* 312:1168–1171.
47. Han Z, et al. (2019) Preparation and evaluation of ZD2 peptide ^{64}Cu-DOTA conjugate as a positron emission tomography probe for detection and characterization of prostate cancer. *ACS Omega* 4:1185–1190.
48. Yu M, et al. (2018) Nanoparticles targeting extra domain B of fibronectin-specific to the atherosclerotic lesion types III, IV, and V-enhance plaque detection and cargo delivery. *Theranostics* 8:6008–6024.
49. Santimaria M, et al. (2003) Immunoscintigraphic detection of the ED-B domain of fibronectin, a marker of angiogenesis, in patients with cancer. *Clin Cancer Res* 9:571–579.
50. Borsi L, et al. (2002) Selective targeting of tumoral vasculature: Comparison of different formats of an antibody (L19) to the ED-B domain of fibronectin. *Int J Cancer* 102:75–85.
51. Xie, YJ, et al. (April 1, 2018) Nanobody-based CAR T cells that target the tumor microenvironment inhibit the growth of solid tumors in immunocompetent mice. *Proc Natl Acad Sci USA* 116, 7624–7631.
52. Folkman J (1995) Angiogenesis in cancer, vascular, rheumatoid and other disease. *Nat Med* 1:27–31.